Electronic Supplementary Information

Construction of an aggregation-induced electrochemiluminescent sensor based on aminal-linked covalent organic framework for sensitive detection of glutathione in human serum

Linlin Song,[‡a] Wenqiang Gao,[‡b] Qinru Han,[‡a] Yiping Huang,[‡a] Lin Cui,[*a] and Chun-yang Zhang[*a]

[a] College of Chemistry, Chemical Engineering and Materials Science, Shandong Normal University, Jinan 250014, China.

[b] Beijing National Laboratory for Molecular Sciences, Key Laboratory of Organic Solids, Institute of Chemistry, Chinese Academy of Sciences, Beijing 100190, P.R. China; University of Chinese Academy of Sciences, Beijing 100049, P.R. China.

EXPERIMENTAL SECTION

General.

Piperazine, tetramethylammonium hydroxide, tri-n-propylamine (TPrA), and 4',4''',4'''',4''''''-(1,2-ethenediylidene)tetrakis[1,1′-biphenyl]-4-carboxaldehyde (ETBC) were purchased from Sigma-Aldrich Co., Ltd. (Shanghai, China). Methanol, $MnCl_2$ and dichloromethane were obtained from Sinopharm Chemical Reagent Co., Ltd. (Beijing, China). Phosphate buffer saline (PBS, 0.1 M) was prepared by mixing the stock solutions of NaH_2PO_4 and Na_2HPO_4. All other reagents were of analytical grade and used as received. All aqueous solutions were prepared using ultrapure water obtained from a Millipore water purification system (≥18 MΩ, Milli-Q, Millipore, USA).

Electrochemiluminescent (ECL) experiments were performed using an MPI-EII multifunctional electrochemical and chemiluminescent analytical system (Xi'an Remex Analytical Instrument Co., Ltd. China) with a modified glassy carbon electrode (GCE, 4 mm in diameter, Gaoss Union, Wuhan, China) as the working electrode, a platinum wire as the counter electrode, and an Ag/AgCl electrode (saturated KCl) as the reference electrode. The scanning electron microscope (SEM) images were obtained by using a Sirion-100 (FEI) and a SU-8010 (Hitachi) scanning electronic microscope. The transmission electron micrograph (TEM) images were obtained on a JEOL JEM 2010 electron microscope (JEOL Ltd., Japan). The crystal structure was characterized by using X-ray diffraction (XRD) (Philips, Rigaku D/MAX 2200PC X-ray diffractometer, Cu Kα radiation, Holland). The FT-IR spectra were obtained by using a Thermo Scientific Nicolet iS50 FT-IR spectrophotometer (Hitachi, Japan) equipped with a xenon lamp. X-Ray photoelectron spectroscopy (XPS) was performed on ESCALab 250 X-ray photoelectron spectrometer with a monochromatized Al Ka X-ray source (1486.71 eV). Absorption spectra were obtained by using a pharmaspec UV-3900 UV-visible spectrophotometer (Hitachi, Japan). Nitrogen sorption isotherm measurements were performed on a Kubo-X1000 multi-analysis station automatic physical adsorption analyzer (Beijing Builder Electronic Technology Co., Ltd. Beijing, China) at 77 K. The obtained nitrogen sorption isotherms were evaluated to determine the pore properties including BET specific surface area, pore size distribution, and total pore volume. UV-vis diffuse reflectance spectrum (DRS) was obtained by using UV-2450 UV-vis

spectrophotometer (Shimadzu, Tokyo, Japan).

Synthesis of the A-COF.

The 4',4‴,4⁗,4‴‴'-(1,2-ethenediylidene)tetrakis[1,1′-biphenyl]-4-carboxaldehyde (ETBC) (24.0 mg, 0.0320 mmol) and piperazine (10.14 mg, 0.128 mmol) were added in toluene (1 mL) in a glass ampoule. The ampoule was sealed after being degassed in a liquid nitrogen bath for 20 min, warmed to room temperature, and then kept at 120 $^{\circ}$C without disturbance for 3 days to yield a yellow solid at the bottom of the ampoule. After cooling to room temperature, the solvent was decanted and the solid was washed with anhydrous dichloromethane for 3 times, followed by drying under dynamic vacuum at 80 $^{\circ}$C for 2 h to obtain a yellow powder (25.2 mg, 77.0%), which was insoluble in water and common organic solvents such as acetone, ethanol and N, N-dimethylformamide.

Preparation of MnO$_2$ nanosheets.

The 20 mL of an aqueous solution containing 3 wt % H$_2$O$_2$ and 0.6 M tetramethylammonium hydroxide were prepared and then added to 10 mL of 0.3 M MnCl$_2$ solution quickly within 15 s. The solution became dark brown immediately and was left to be stirred vigorously overnight in the open air at room temperature. The obtained bulk manganese dioxide was centrifuged at 2000 rpm for 20 min and then washed with water and methanol. Subsequently, the bulk manganese dioxide was dried in a drying oven at 60 $^{\circ}$C and kept in a centrifuge tube for further experiments. To prepare the MnO$_2$ nanosheets, 10 mg of bulk manganese dioxide was dispersed in 20 mL of water and ultrasonicated for at least 10 h, followed by centrifuging at 2000 rpm for 30 min. The resultant supernatant was kept for further use.

Preparation of the A-COF Modified GCE and the ECL Measurements.

The bare GCE was modified with 0.02 mg mL^{-1} A-COF in DMF solution, followed by drying at room temperature to obtain the A-COF/GCE. The anodic ECL of the A-COF was obtained at the potential of 0 ~ +1.2 V with photomultiplier tube set at 600 V. The scan rate was 300 mV s^{-1} unless

specifically noted.

Detection of GSH.

The 20 μL of MnO_2 (0.2 mg mL^{-1}) was dripped onto the A-COF/GCE. After airing, the MnO_2/A-COF/GCE was immersed in various concentrations of GSH and reacted for 40 min, followed by washing with PBS solution (10 mM, pH 7.4). The ECL emission was recorded at potential from 0 to +1.2 V.

Detection of GSH in Human Serum Samples.

The human serum samples were centrifuged at 10000 rpm for 10 min. Then 100 μL of supernatant was extracted and spiked with 100 μL of GSH standard solution (0.1 μM, 1.0 μM, and 10.0 μM), respectively, followed by ECL measurements. The experiments were carried out in triplicate. ECL measurements were performed as described above.

ECL Quantum Efficiency.

Relative ECL efficiency was measured based on equation S1.[1]

$$\Phi_{ECL} = \Phi_{ECL}^0(I/Q)/(I^0/Q^0) \qquad (S1)$$

where Φ_{ECL} and $\Phi^0{}_{ECL}$ are the ECL efficiency of the A-COF and $Ru(bpy)_3^{2+}$, I and I^0 are the integrated ECL intensities of A-COF and $Ru(bpy)_3^{2+}$, and Q and Q^0 are the consumed charges of the A-COF and the standard, respectively.
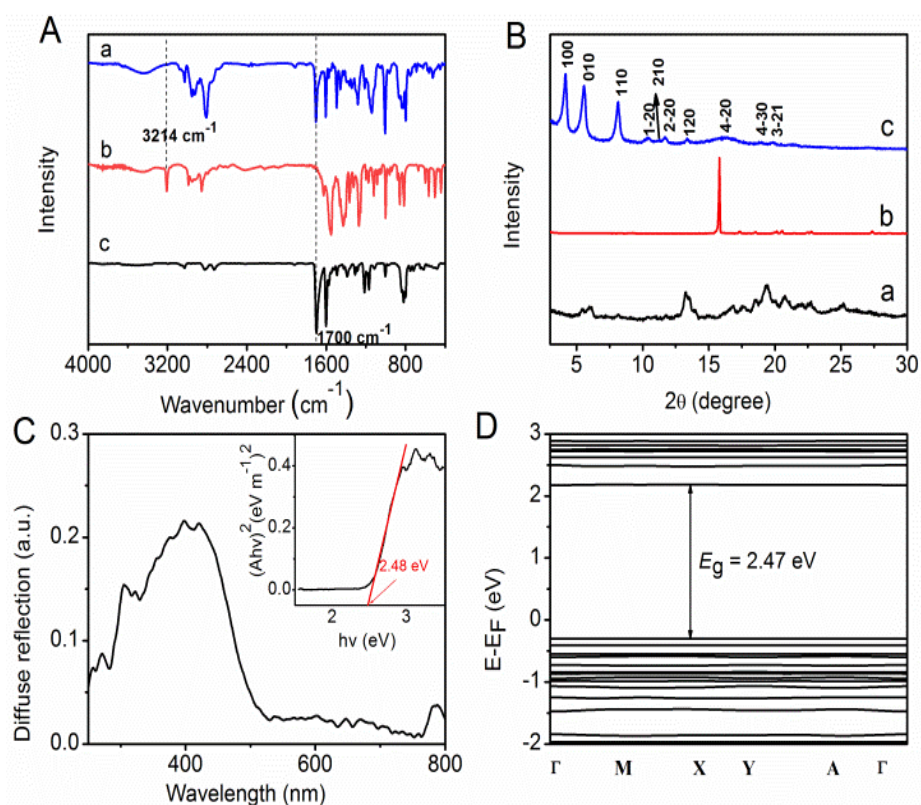
Characterization of the Synthesized Materials.

Figure S1. (A) FT-IR spectra and (B) XRD patterns of ETBC (a), piperazine (b), and A-COF (c); (C) Diffuse reflectance spectrum (DRS) of the A-COF. The inset of (C) shows the Tauc plot of the A-COF; (D) Band structure of the A-COF.

The polymer structure was characterized by Fourier transform infrared (FT-IR) spectroscopy (Figure S1A). In comparison with ETBC (Figure S1A, curve a), piperazine (Figure S1A, curve b), no vibration band corresponding to the N-H group of piperazine (3214 cm^{-1}) is observed and the peak assignable to aldehyde group (1700 cm^{-1}) is dramatically attenuated in the IR spectra of the A-COF (Figure S1A, curve c), suggesting high degrees of conversions of the monomers. No vibration peak of C=N shows up, indicating there are no imine linkage in the obtained materials. The crystal structure of A-COF is elucidated by using powder X-ray diffraction (XRD). The high quality of the XRD patterns offer direct acquisition of crystal lattice parameters of the A-COF (Figure S1B). Three high intense diffraction peaks at 4.24°, 5.68° and 8.27° are attributed to (100), (010) and (110) facets, respectively. Another six weak peaks at 10.49°, 11.87°, 13.53°, 16.40°, 18.95° and 19.98° are assignable to (1-20), (210), (120), (4-20), (4-30) and (3-21) facets,

respectively. The UV−vis diffuse reflectance spectrum (DRS) shows that the A-COF possesses strong absorption in the range of 200–800 nm (Figure S1C), with the band gap energy (E_g) being calculated to be 2.48 eV (inset of Figure S1C) [2] according to equation S2.

$$\alpha h\nu = A\left(h\nu - E_g\right)^{1/2} \tag{S2}$$

where ν represents the light frequency, α represents the absorption coefficient, h represents the Planck constant, E_g represents the band gap, and A represents a constant term.

The calculated electronic band structures of the A-COF along the symmetry line in the Brillouin zone from Γ to M, X, Y and A are demonstrated in Figure S1D. Distinct from graphene, flat bands exist near the Fermi energy level, further confirming that the A-COF is a semiconductor. Moreover, the band gap of the A-COF (2.47 eV) is consistent with DRS band gap (2.48 eV) (Figure S1C).
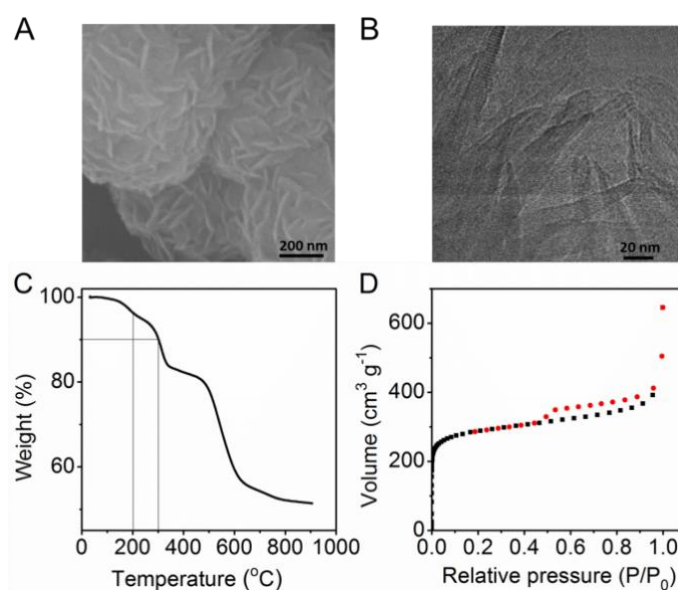

Figure S2. (A) SEM and (B) TEM images of the A-COF; (C) Thermogravimetric analysis (TGA) of the A-COF and (D) Nitrogen adsorption and desorption isotherms of the A-COF measured at 77 K.

The morphology of the A-COF was characterized by scanning electron microscopy (SEM) (Figure S2A) and high-resolution transmission electron microscopy (TEM) (Figure S2B). The SEM image reveals that the A-COF displays the agglomerates of flake-like structures (Figure S2A). The TEM image further indicates the layered structure of the A-COF (Figure S2B).

Thermogravimetric analysis (TGA) reveals almost 5% weight loss before 200 °C and 10% weight loss around 350 °C for the A-COF, indicating the good thermal stability of the A-COF (Figure S2C). Brunauer-Emmett-Teller (BET) measurement was used to analyze the porous structure of the A-COF. As shown in Figure S2C, the A-COF exhibits both type-I and type-IV adsorption branches. The sharp nitrogen gas uptake at a low pressure indicates the formation of the microporous A-COF network. The enhanced nitrogen uptake at $P/P_0 > 0.9$ without saturation in the adsorption isotherm is attributed to the formation of pores induced by polymerization.[3] The Brunauer−Emmet−Teller (BET) specific surface area is calculated to be 936 $m^2\ g^{-1}$ (Figure S2D).
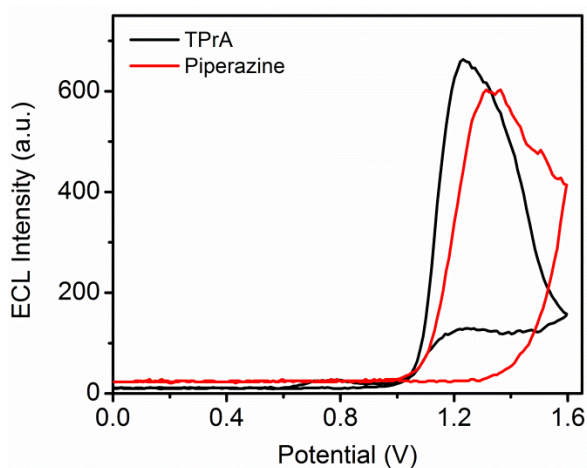

Figure S3. ECL−potential curves of bare GCE in 0.1 M PBS (pH 7.4) containing 10 mM TPrA (black) and 10 mM piperazine (red), respectively.
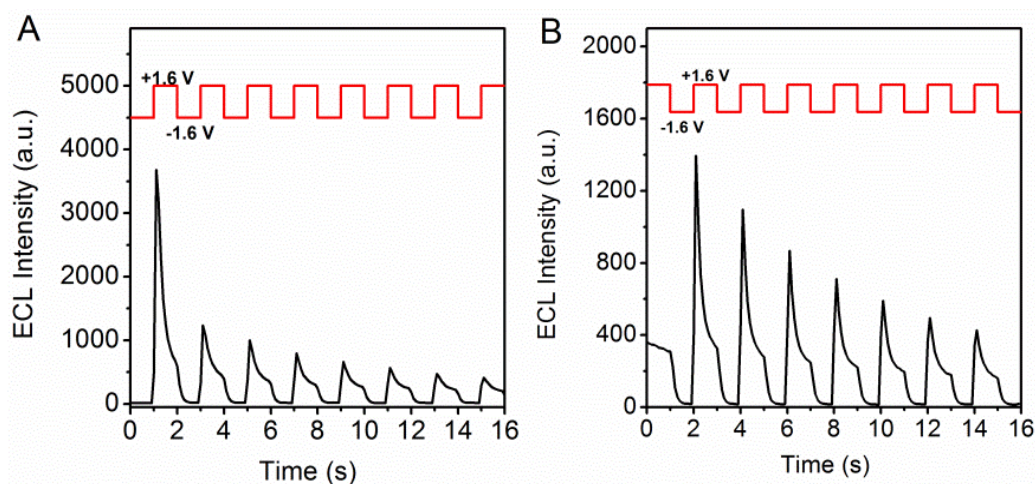
Annihilation ECL of the A-COF-Modified GCE.

Figure S4. (A and B) ECL transients of the A-COF modified GCE in N_2 -saturated PBS by stepping pulse from -1.6 V to +1.6 V (A), and from +1.6 V to -1.6 V (B) in the nitrogen-saturated 0.1 M PBS.

Annihilation ECL activity of the A-COF was further investigated by applying a 1 Hz potential step between cathodic and anodic potentials (Figure S4A and S4B). The oxidative process-initiated ECL transient of the A-COF/GCE is shown in Figure S4A. When stepping the A-COF/GCE at -1.6 V for 1 s in the initial step, no distinct ECL signal is detected due to the injection of only electrons into the LUMO of the A-COF (Figure S4A). When alternately stepping the A-COF/GCE from +1.6 V to -1.6 V, a distinct ECL signal is detected (Figure S4A), following the annihilation mechanism (eqs. S3-S6). The A-COF on the electrode is firstly reduced to the A-COF$^{-\bullet}$ at -1.6 V (eq. S3), then the A-COF on the electrode is oxidized to the A-COF$^{+\bullet}$ at +1.6 V (eq. S4). Notably, the A-COF$^{\bullet+}$ and A-COF$^{-\bullet}$ are generated at oxidation and reduction potentials, respectively. The reaction of the A-COF$^{+\bullet}$ with the A-COF$^{-\bullet}$ generates the A-COF* (eq. S5). When the A-COF* decays back to the ground state, a high ECL emission at +1.6 V is produced (eq. S6). However, the rapid decrease of the ECL emission is observed at +1.6 V, with very low intensity in the follow potential steps from -1.6 and +1.6 V, confirming the stable of reduced form of A-COF (A-COF$^{-\bullet}$).

$$\text{A-COF} + e^- \rightarrow \text{A-COF}^{-\bullet} \qquad\qquad\qquad (S3)$$

$$\text{A-COF} - e^- \rightarrow \text{A-COF}^{+\bullet} \qquad\qquad\qquad (S4)$$

$$A\text{-}COF^{+\bullet} + A\text{-}COF^{-\bullet} \rightarrow A\text{-}COF^* \tag{S5}$$

$$A\text{-}COF^* \rightarrow A\text{-}COF + h\nu \tag{S6}$$

The reductive process-initiated transient ECL of the A-COF/GCE is shown in Figure S4B. When the potential starts at +1.6 V for 1 s, a distinct ECL is detected upon stepping the A-COF/GCE from +1.6 V to -1.6 V. A low ECL emission of the A-COF/GCE is detected at the starting potential of +1.6 V compared with that obtained by stepping the A-COF/GCE from -1.6 V to +1.6 V. This can be ascribed to the reaction of A-COF$^{+\bullet}$ with the trace amount of OH$^-$ in water acting as an electron donor to produce light emission.[4,5]

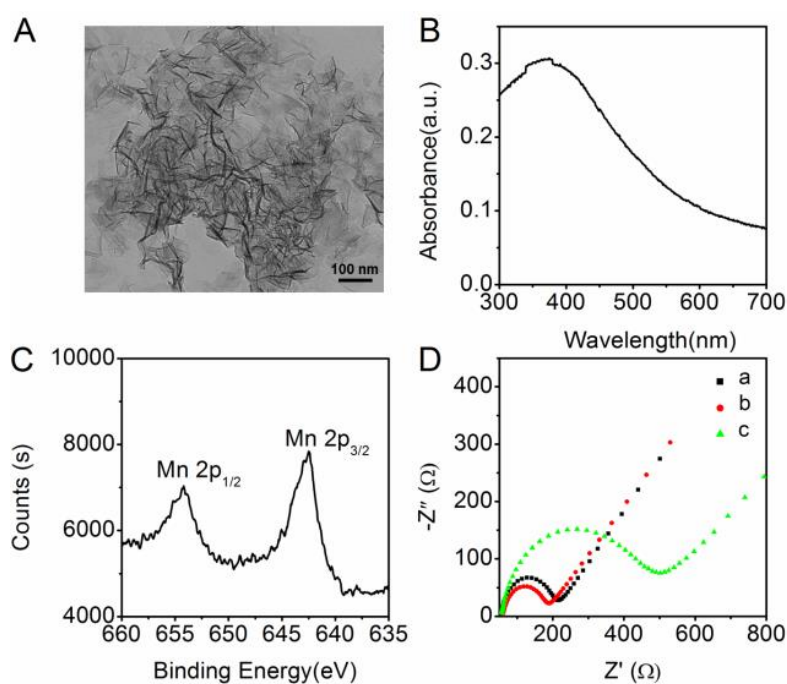**Characterization of MnO$_2$ nanosheets, A-COF/GCE, and MnO$_2$/A-COF/GCE**

Figure S5. (A) TEM image of MnO$_2$ nanosheets. (B) UV-vis absorption and (C) XPS spectrum of MnO$_2$ nanosheets. (D) EIS characterization obtained from (a) bare GCE, (b) A-COF/GCE and (c) MnO$_2$/A-COF/GCE in 0.1 M KCl containing 5 mM [Fe (CN)$_6$]$^{3-/4-}$ solution.

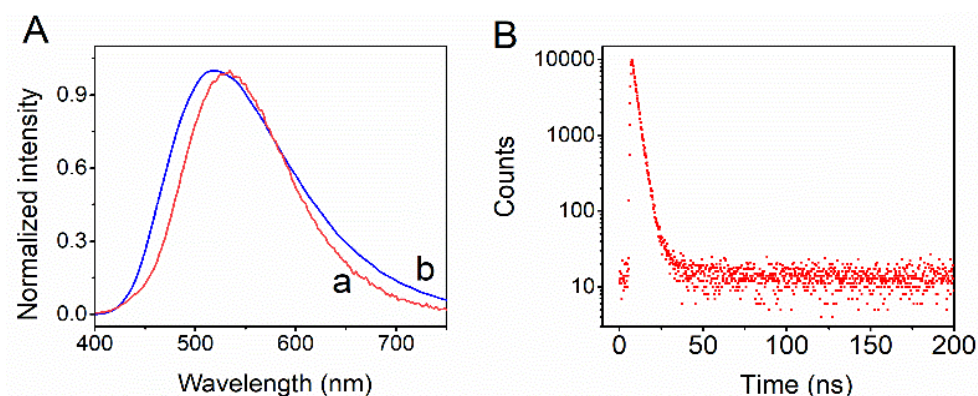**ECL spectrum of the aminal-COF/TPrA System**

Figure S6. Normalized photoluminescence spectrum of the A-COF (a) and anodic ECL spectrum of the A-COF in PBS + 10 mM TPrA (b). (B) Time-resolved luminescence decay curve of the A-COF under 405 nm excitation.

The ECL spectrum of the A-COF/TPrA system was recorded in the potential range from 0 to +1.2 V. The photoluminescence peak (Figure S6A, curve a) of the A-COF (530 nm) and the ECL spectrum of the A-COF modified GCE at +1.2 V shows a peak at 520 nm in 10 mM TPrA + 0.1 M PBS (Figure S6A, curve b). The transient ECL spectrum (Figure S6A, curve b) is identical with the photoluminescence spectrum (Figure S6A, curve a) of the A-COF, suggesting band-gap ECL model with the same excited states for both the transient ECL and photoluminescence spectra.[6] The lifetime of the A-COF is determined to be 2.85 ns under 405 nm excitation (Figure S6B, red).
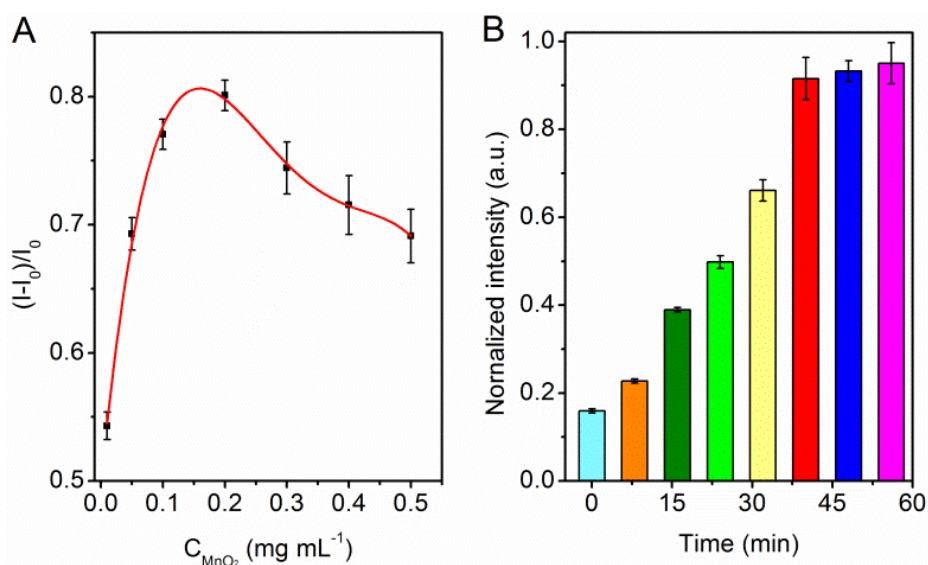
Optimization of Experimental Conditions.

Figure S7. (A) Optimization of the MnO_2 concentration, and (B) the reaction time. The GSH concentration is 100.0 μM. Error bars are standard derivation obtained from three independent experiments.

To acquire the high assay performance, we optimized the reaction parameters including the concentration of MnO_2 nanosheets and the reaction time. Figure S7A shows the effect of the MnO_2 concentration upon the ECL intensity of the A-COF/GCE after incubation in 100.0 μM GSH solution. The recovery efficiency is calculated according to E (%) = $(I/I_0 - 1) \times 100\%$, where I is the ECL intensity in the presence of GSH and I_0 is the ECL intensity in the absence of GSH. The recovery efficiency is measured to be 80% at the MnO_2 nanosheets concentration of 0.2 mg mL^{-1}. Thus, 0.2 mg mL^{-1} MnO_2 nanosheets are used in subsequent researches. After adding 100.0 μM GSH into the MnO_2/A-COF/GCE, the ECL intensity gradually increases with the reaction time and reaches the maximum value at 40 min (Figure S7B). Thus, the reaction time of 40 min is used in subsequent researches.
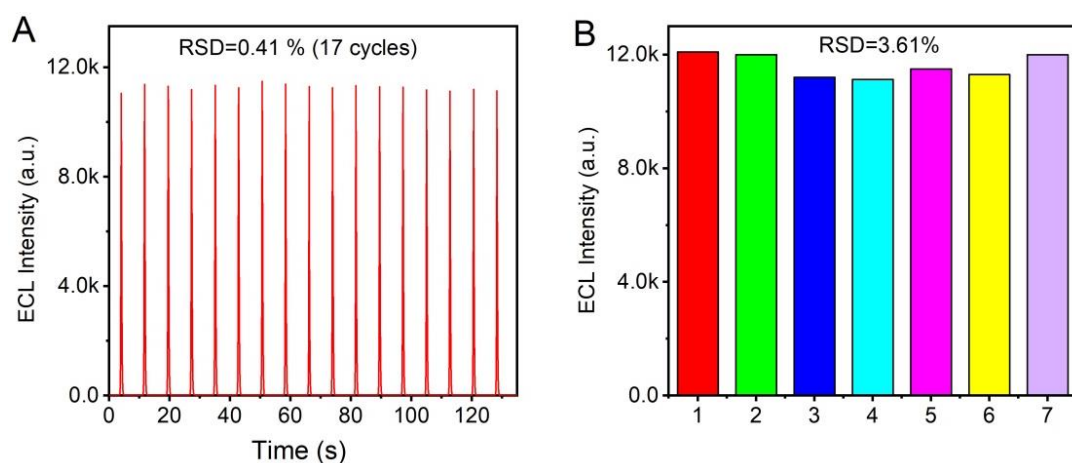
Reproducibility and Stability of the ECL Sensor.

Figure S8. (A) Stability assessment of the ECL sensor by continuous scanning for 17 cycles. Scan rate is 0.30 V s^{-1}. (B) Reproducibility of the ECL sensor for the measurement of 100.0 μM GSH under identical conditions (n = 7).

The stability of the ECL biosensor was investigated by measuring 100.0 μM GSH under consecutive 17-cycle scans (Figure S8A). Stable and continuous ECL signals with a relative standard deviation (RSD) of 0.41% are obtained even after 17 CV cycles, suggesting the excellent stability of the ECL sensor. The reproducibility of the ECL sensor was studied by measuring 100.0 μM GSH with seven electrodes fabricated under identical conditions (Figure S8B). The RSD is measured to be 3.61%, suggesting the good reproducibility of the ECL sensor.

Table S1. Comparison of the proposed ECL sensor with the reported methods for GSH detection.

Detection methods	Linear range (µM)	Detection limit (nM)	Refs
Electrochemiluminescence	0.05 – 100	17	This work
Electrochemiluminescence	0.2 – 100	50	3
Electrochemiluminescence	5 – 215	330	7
Fluorometry	1 – 200	130	8
Fluorometry	0.5 – 250	160	9
Fluorometry	0 – 350	1500	10
Fluorometry	5 – 50 and 150 - 800	2960	11
Fluorometry	10 – 500	3250	12
Electrochemical	1 – 50 and 100 - 1800	30	13
Electrochemical	1 – 12.5	140	14
Electrochemical	0.4 – 16.4	200	15
Photoelectrochemical	0.5 – 40	100	16

Table S2. Recovery studies in serum samples.

Added (µM)	ECL intensity (a.u.)	Measured (µM)	Recovery (%)	RSD (%)
0.1	4345	0.11	113.1	2.2
1.0	6580	0.98	97.5	0.9
10.0	9050	10.5	105.4	1.6

REFERENCES

1. K. Chu, J. R. Adsetts, J. Ma, C.-Y. Zhang, M. Hesari, L.-Q. Yang and Z.-F. Ding, *J. Phys. Chem. C*, 2021, **125**, 22274-22282.

2. L. Cui, J.-Z. Shen, S.-Y. Ai, X.-L. Wang and C.-Y. Zhang, *Biosens. Bioelectron.*, 2020, **168**, 112545.

3. X.-L. Fu, F. Hou, F.-R. Liu, S.-W. Ren, J.-T. Cao, Y.-M. Liu, *Biosens. Bioelectron.*, 2019, **129**, 72-78.

4. M.-T. Ge and H.-Z. Liu, *J. Mater. Chem. A*, 2016, **4**, 16714-16722.

5. K. M. Molapo, A. Venkatanarayanan, C. M. Dolan, U. Prendergast, P. G. Baker, E. I. Iwuoha, T. E. Keyes and R. J. Forster, *Electrochem. Commun.*, 2014, **48**, 95-98.

6. T.-T. Zhao, Q. Zhou, Y.-Q. Lv, D. Han, K.-Q. Wu, L.-F. Zhao, Y.-F. Shen, S.-Q. Liu and Y.-J. Zhang, *Angew. Chem. Int. Ed.*, 2020, **59**, 1139-1143.

7. R. Zhang, X. Zhong, A.-Y. Chen, J.-L. Liu, S.-K. Li, Y.-Q. Chai, Y. Zhuo and R. Yuan, *Anal. Chem.*, 2019, **91**, 3681-3686.

8. Z.-Z. Dong, L.-H. Lu, C. N. Ko, C. Yang, S.-G. Li, M. Y. Lee, C. H. Leung and D. L. Ma, *Nanoscale*, 2017, **9**, 4677-4682.

9. C. Peng, H.-H. Xing, X.-X. Fan, Y. Xue, J. Li and E.-K. Wang, *Anal. Chem.*, 2019, **91**, 5762–5767.

10. X.-J. Kong, S. Wu, T.-T. Chen, R.-Q. Yu and X. Chu, *Nanoscale*, 2016, **8**, 15604-15610.

11. Y. Li, L.-B. Zhang, Z. Zhang, Y. Liu, J. Chen, J. Liu, P.-Y. Du, H.-X. Guo and X.-Q. Lu, *Anal. Chem.*, 2021, **93**, 9621–9627.

12. J.-S. Lou, Y.-P. Jin, Y.-M. Guo and Q. Li, *Inorg. Chem. Commun.*, 2022, **138**, 109307.

13. A. Safavi, N. Maleki, E. Farjami and F. A. Mahyari, *Anal. Chem.*, 2009, **81**, 7538–7543.

14. M. C C Areias, K. Shinizu and R. G Compton, *Analyst*, 2016, **141**, 2904-2910.

15. H. Tang, J.-H. Chen, L.-H. Nie, S.-Z. Yao and Y.-F. Kuang, *Electrochim. Acta*, 2006, **51**, 3046-3051.

16. G.-H. Chen, J.-L. Wang, C.-Y. Wu, C.-Z. Li, H. Jiang and X.-M. Wang, *Langmuir*, 2012, **28**, 12393–12399.